RESEARCH ARTICLE

Bioinspired Multi-material Polyjet-printed Frog Robot for Synchronous and Asynchronous Swimming

Afaque Manzoor Soomro[1,2] · Jae-Wook Lee[1] · Fida Hussain Memon[1,2] · Faheem Ahmed[1] · Kashif Hussain[2] · Kyung Hyun Choi[1]

Abstract
This paper proposes the bioinspired soft frog robot. All printing technology was used for the fabrication of the robot. Polyjet printing was used to print the front and back limbs, while ultrathin filament was used to print the body of the robot, which makes it a complete soft swimming robot. Dual thrust generation approach has been proposed by embedding the main muscle and antagonistic muscle in all the limbs, which enables it to attain high speed (18 mm/s), significant control to swim in dual mode (synchronous and asynchronous modes). To achieve the swimming motion of frog, four SMA (BMF 300) muscle wires were used. The frog robot is named as (FROBOT). The hind limbs are 60 mm long and 10 mm thick on average, while the front limbs are 35 mm long and 7 mm thick. Model-based design and rigorous analysis of the dynamics of real frogs have allowed FROBOT to be developed to swim at a level that is remarkably consistent with real frogs. Electrical and mechanical characteristics have been performed. In addition, the test data were further processed using TRACKER to analyze angle, displacement and velocity. FROBOT (weighs 65 g) can swim at different controllable frequencies (0.5–2 Hz), can rotate in any direction on command from custom built LabVIEW software allowing it to swim with speed up to 18 mm/s on deep water surface (100 cm) with excellent weight balance.

Keywords Bioinspired · Soft robotics · Frog · FROBOT · Asynchronous swimming

1 Introduction

Soft robotics is incipient research area with wide range of new applications such as fully integrated soft octobot, octopus robot [1], worm robot [2, 3] and soft multi-comotion microbot [4]. For under water exploration, inspection, observation and rescue developing swimming robots with intrinsically soft materials and achieving flexibility with numerous degrees of freedom in their motion, have gradually attracted the attention of bionics [5]. Soft robots are expeditiously discovering new perspectives of typical robotic actions for instant, locomotion quickness in manipulation, clutching,

morphing, self-healing and so on [6–11]. Soft robotics has a new directions with vast exploration of underwater life with close interactions using biomimetic creatures, which are capable of athletic swimming maneuvers [12–14].

The frog-inspired robots have acquired an excellent value due to frog's amphibian nature. Currently, many experimental-based studies on frog-inspired swimming and jumping robots based on modeling analysis and swimming mechanism have been reported [15–17]. These robots are relatively large in dimensions, complex in design aspects and a bit heavy, which makes robots relatively impossible to actually realize the swimming and jumping mechanism [6].

Recent advancements in intelligent materials have made easy for their use as soft actuators due to their distinct and matchless soft characteristics [14]. For instant, shape-memory alloys materials have been at front end for last few years due to its characteristic of lacking in mechanical parts [18] or the capacity to upgrade the mechanical movables with the application of current with different rating relevant to dimensions of SMA used [19, 20] The intelligent material such as SMA [13, 14, 21] has made it

✉ Afaque Manzoor Soomro
    afaquemanzoor@gmail.com

✉ Kyung Hyun Choi
    amm@jejunu.ac.kr

1 Department of Mechatronics Engineering, Jeju National University, Jeju 63243, South Korea

2 Department of Electrical Engineering, Sukkur IBA University, Sukkur 65200, Pakistan

possible for soft robots to become much capable of following animal movements. However, conventional stiff mechanical systems for robots are complex and it is more difficult to develop miniaturized mechanical systems to achieve desired animal motion in under water environments. SMAs are mostly available in wires, pipes, springs and ribbons types [14, 16].

In literature, numerous soft robots have been developed enabling proprioception based on shape memory alloy actuators [17, 22]. One of the SMA-based soft robots is developed which uses micro meter range diameter SMA wire as an actuator, in concurrence with fully 3D-printed hand for prosthesis application, it is light weight with flexible geometrical shape to attain silent movements [23–27]. Another interesting development is earthworm soft robot with fluid-filled structure surrounded by muscular body which behaves more likely as real earthworm. This soft robot is mainly built with two viscoelastic silicon rubber elements which imitates a constant volume hydrostatical structure [13] causing peristaltic locomotion using radical twisting and bending of soft hydrostatical elements [28]. These hydrostatical elements are being energized through applying pressure to spring-shaped SMA wires [3, 5, 29–34]. Recently a soft actuator is also developed to achieve an autonomy in soft fish robot which is energized by an on board power source [8]. The modeling and fabrication of this robot reflects the robot performance with swift responses [8, 15, 35]. The frog, among other aquatic organisms, has a crucial attribute for not only excellent swimming, these hydrostatic segments, but it can also walk on land. However, designing a robot with soft materials for an underwater environment is rather difficult [16, 36, 37]. On other end, dielectric elastomers [7], a class of electroactive polymer, are used for actuation mechanism for different soft robots [38, 39], these are sandwich-like structure with elastomer membrane between two compliant electrodes [7]. These elastomers then behave as electromechanical transducer; when applying voltage on compliant electrodes, an attractive electrostatic force suppresses the membrane resulting the thickness reduction and area expansion of the membrane [6, 18, 40–42].

Herein, we propose the design, fabrication and characterization of frog robot (FROBOT) that is capable of swimming underwater in synchronous and asynchronous modes. The robot was designed by printing its muscle wires embedded front and back limbs using PolyJet printing process. Whereas the body of the robot was printed using custom-made multi-header printing system which also placed the muscle wires during the printing phase. Dual thrust approach was implemented which enabled the FROBOT to swim in both modes with the maximum speed of 18 mm/s at 1.5 Hz. The rigorous analysis, such as of angle of actuation, displacement and velocity curves was performed and compared with that of real frog swimming dynamics. Nature-inspired experimental

setup was also designed which was fully controllable using in-house made software. The proposed robot showed remarkable consistency in biomimicking the real frog locomotion with the power supply of 5 V 1A.

2 Experimental

A custom-made fully controllable setup was developed for the experimentation demonstration of the fabricated FROBOT. An artificial transparent glass tank with volume ($1 \times 2 \times 1$ m^3) was infilled with water up to 75% of its maximum capacity. It was decorated with the artificial grass and plants to significantly mimic the real frog swimming environment. The weight of FROBOT was 130 g. Before the printing of the robot, the buoyancy effect was critically analyzed and different necessary weights at different points were added at the modeling phase after considering the possible hindrances of connecting wires. This enabled the printed robot to balance its weight under water without further calibration. For the provision of power to the robot, ultra-thin wires were used which added negligible obstacle to the swimming. The muscle wires in of different diameters (0.1, 0.15, 0.2 and 0.3 mm) were purchased from SMARTWIRES. After the performance characterization of all these four muscle wires, all the experiments were carried out using 0.3-mm-diameter wire. The stimulation for the actuation was done using 5 V, 1A power supply, which could easily rise the temperature of wire to 70 °C (austenite temperature). Figure 1b shows the detailed schematic of the setup. The current driver circuits were used to provide the power using controlled pulse width modulation (PWM) generated by myRIO board. The entire setup was directly controlled and monitored using the custom-made LabVIEW Software (Version 2019). The user can monitor the temperature robot's limbs, tank water, real-time videos recorded using two high-definition camera, heat distribution using IR thermal camera.

2.1 Fabrication Process

The fabrication of FROBOT was done using multi-step all-printed technology. For the functionally responsive front and back limbs, the polyJet printing was used. This process uses ultraviolet (UV) radiation to cure sprayed acrylic photopolymer layers. The jetting head is formed by a matrix of jetting orifices disposed along the *Y* axis and is mounted on a carriage that allows for *X* forth-and-back displacements and alternate transverse (*Y*) relocations. Additionally, the manufacturing tray can move in the vertical (*Z*) direction, after each layer has been successfully manufactured. As shown in Fig. 1a, the first half part of all four limbs were printed which then were brought to custom-made multi-header printing system which inserted the muscle wires

Fig. 1 **a** Step-by-step FRO-BOT manufacturing process, **b** Schematic of the experimental equipment. Here, we monitor the experiment using two high-resolution imaging devices, a thermal imaging camera that monitors real-time temperature, and myRIO, which monitors and controls the entire setup
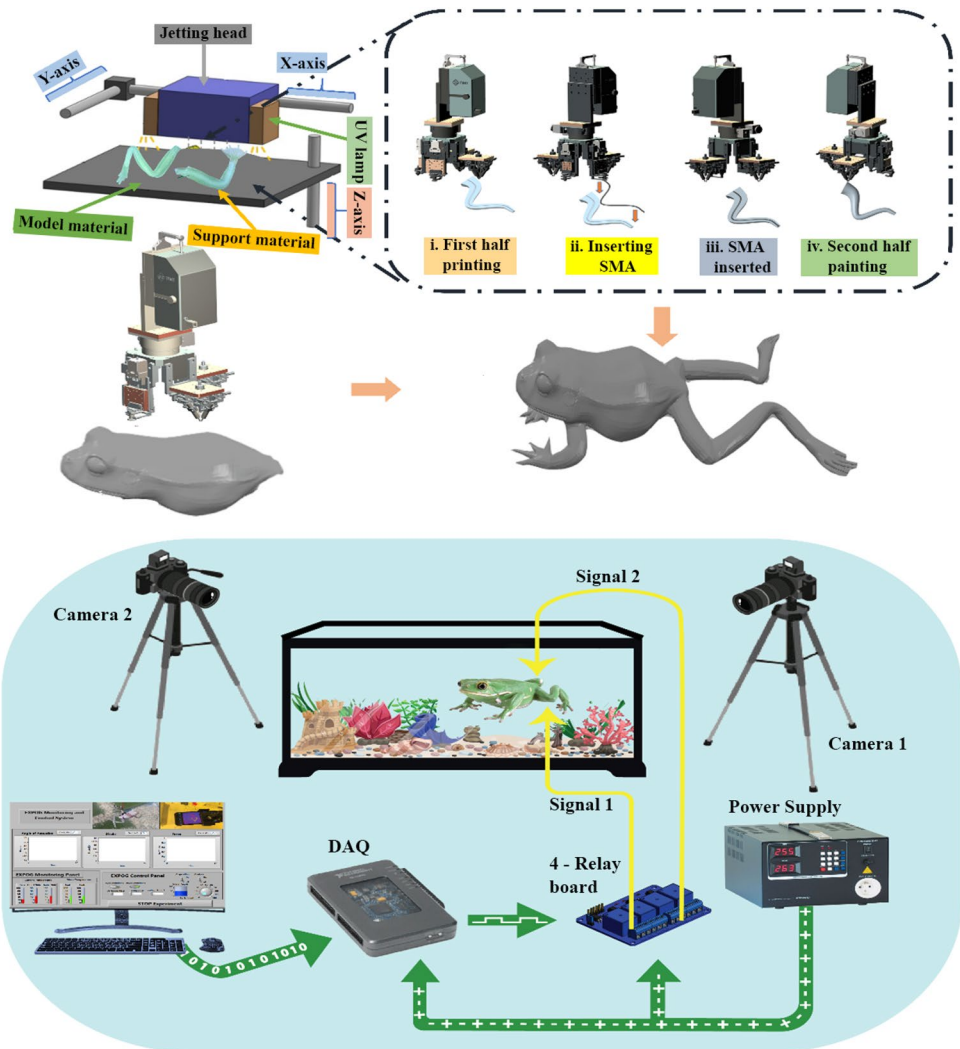
and necessary connections and sent back to PolyJet printing setup which printed the second half of the limbs. In parallel, the body of the frog robot was printed using multi-header system. Herein, ultraflex filament (BLACKMAGIC3D, 1.75 mm) was used. The system was loaded with a CAD model of proposed robot design, which was fully optimized using simulation and mathematical work, as carried out in our previous work. The high-definition camera included with the printing system was used to continuously monitor the entire operation. The introduction of feedback sensors, including imaging devices, helped to prevent printing errors.

3 Results and Discussion

The Anura, like RANA Esculenta, served as an inspiration for the design of the FROBOT (semi-aquatic frog). This infers that the proposed robot must be soft, bioinspired and follows the swimming mechanism. Like the natural frog, which swims by its contraction and expansion of different muscles for effective and controllable swimming, the FRO-BOT follows the same by using dual-thrust approach. The thrust motion was intended to continuous swimming of the FROBOT by exploiting the dual muscles embedded inside each limb. The main muscle develops the thrust (abrupt) force necessary for the action force for water. In return, the fluidic friction of water pushes the robot in the forward direction. Similarly, in order to relax the limb, the second muscle is activated which produces the negative force for dragging the limb to its original position. Moreover, for this force generation, it was made sure that both muscles are not simultaneously activated; there must be significant delay which will protect the muscles life, in addition to attaining maximum swimming speed. For making a complete soft robot, polyJet and fused deposition manufacturing printing techniques were used. The functionally responsive front and back limbs of the frog were printed using PolyJet system. The printing process using PolyJet system is explained in

detail in supplementary data. Just after the bottom layer printing of the limbs, it was moved to multi-header system, which was pre-calibrated to place the muscle wires and make necessary connections. Afterwards, the second layer was printed. In parallel, the body of the FROBOT was printed using the same multi-header system with ultraflex filament. In the end, all parts were connected using the soft glue and left in room temperature, till it was completely bonded.

In the proposed design, two degrees of freedom were added: the knee joint and the flipper joint. In each limb, there are two muscles. Figure 2 shows the actuation mechanism of FROBOT. The main muscles are responsible for the drag forces, while the antagonistic muscles create the lift force and enable the limbs and flippers to return their original positions. The sequential control of these muscles are time-bound and are activated when the other muscles are off. A deliberate delay of few hundred milli seconds has been added in the software to ensure the settling of each muscle wire.

In order to make sure, the muscle wires get the required heat level and the overall body of the frog is not damaged. The thermal characterization was carried out using IR thermal camera (FLIR ONE), S1Movie. Figure 3a shows the images taken from the video captured by high-definition imaging device. On the application of voltage to the FROBOT, the current starts flowing which causes the temperature to rise. A gradual increase in the heat can be seen in both, the front and back limbs. As a result of the muscular wires being imbedded in the limbs, the temperature increase may appear to be intermittent, but it really

takes time for the limbs to reach their maximum temperature. The FROBOT gains an advantage from this as well because it has no discernible impact on the temperature of the water in which it swims.

The selection of a specific muscle wire with diameter plays important role, such as the thrust generation, temperature rise and resistance of the wires at specific time. For this, three muscle wires with diameter of 0.1, 0.2 and 0.3 mm were heated using 5 V 1A supply. As shown in Fig. 3b, the wire with 0.3 mm has relatively better heating response and proves to be better candidate for precise control of the speed and its ability for long life. Moreover, Fig. 3c shows the temperature response of 0.3 mm muscle wire against different current supply. Based on the results, 1A, being the better supply was selected. Resistance of the muscle wire, in addition to the temperature, was used for the feedback, which enabled the control of speed and direction of the swimming (asynchronous swimming). Figure 3d shows the resistance response of different muscle wires against increase in the temperature. Although there is not a big difference in the resistance variations, yet the muscle wire with diameter of 0.3 mm has significantly stable response.

Moreover, the simplified model inspired from natural frog is shown in Fig. 2b. Three angles at the back limbs (hip joint, knee joint and flipper joint) play a significant role in the swimming of the frog. However, for the design of FROBOT, the model was deliberately kept simple with ignoring the hip joint which could have added more complexity to the mode. For the front limbs, only one angle of

Fig. 2 Working mechanism; top left figure displays actuation pattern for synchronous swimming, top right figure displays model of absolute and relative positional taking into account center of mass and absolute frame points, and bottom right figure displays dual approach of thrust generation with full stroke operation (S1 and S3 are the main muscles for lift force generation, S2 and S4 are the antagonistic muscles responsible for drag force generation)
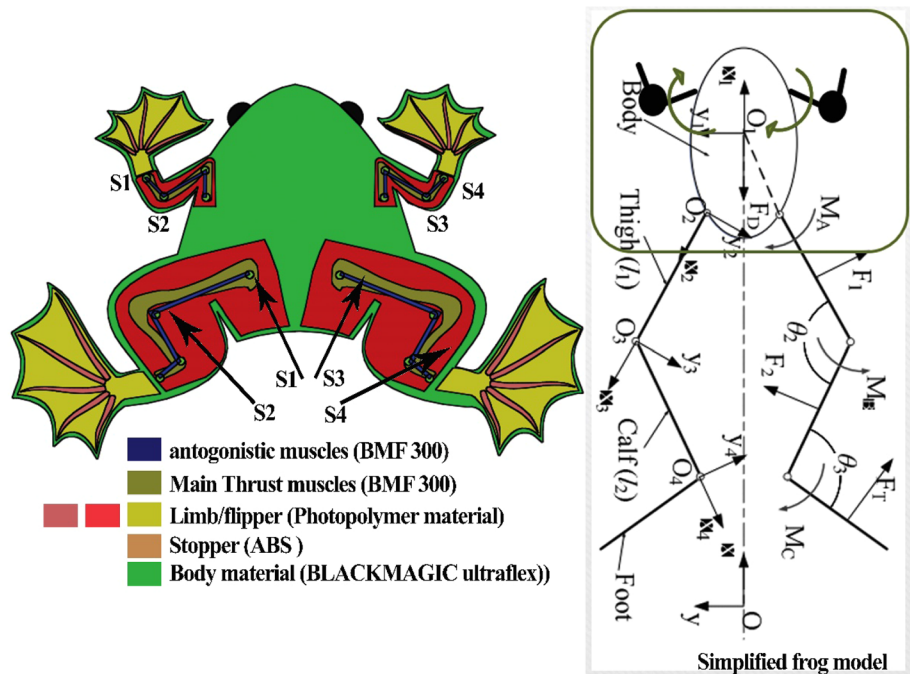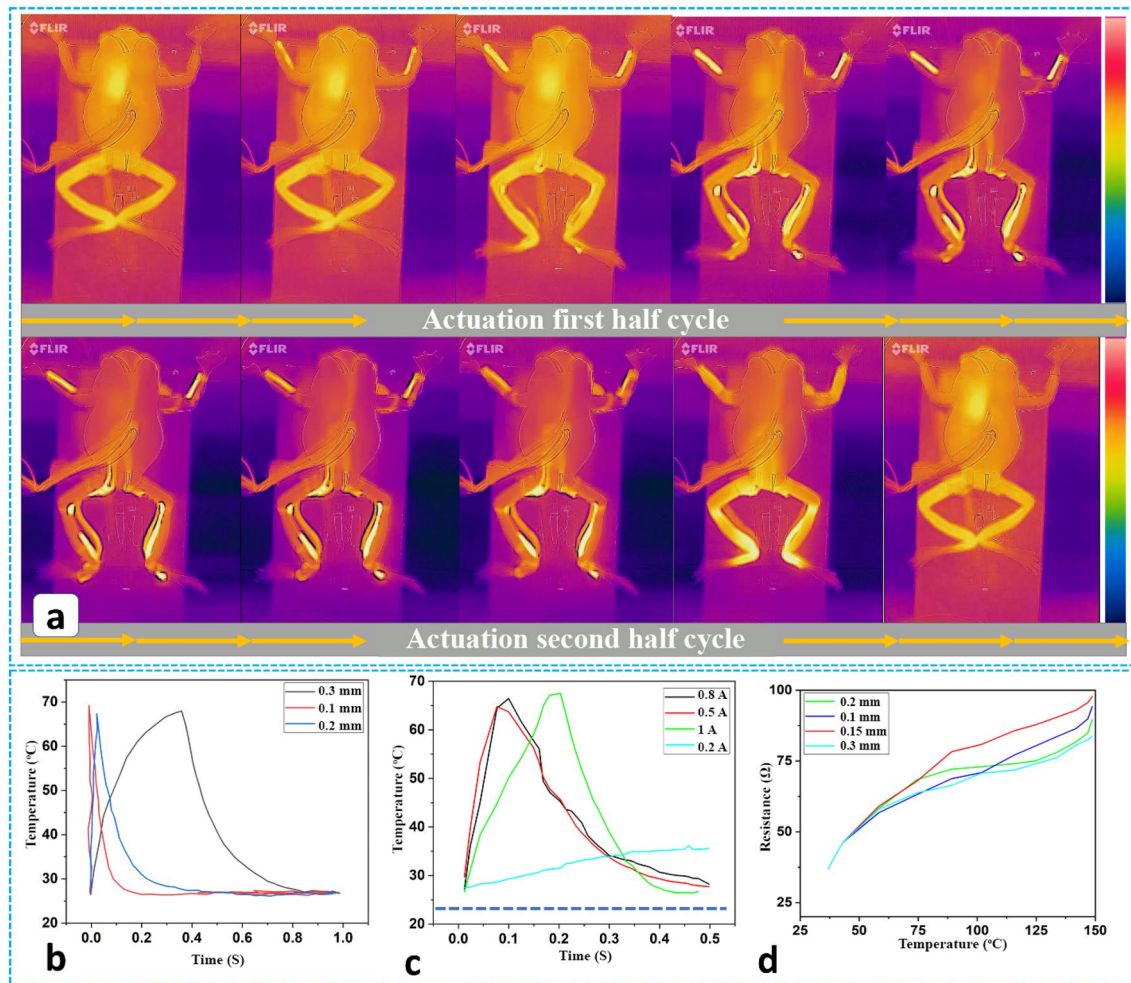
Fig. 3 a Thermal characterization sequential images taken from Smovie1, **b** temperature change of muscle wire (with 0.1, 0.2, 0.3 mm diameter), **c** temperature response against different current supply with voltage being constant, **d** resistance vs temperature of muscle wires with different diameters

limb joint was considered. The force exerted by each limb is dependent on the velocity of exertion as given in Eq. (1).

$$F_{\text{limb}} = F_{\text{max}} \frac{V_{\text{max}} - V_{\text{limb}(t)}}{V_{\text{max}} + G V_{\text{limb}(t)}} \tag{1}$$

F_{limb} being the maximal isometric force of each limb; $V_{\text{limb}(t)}$ the instantaneous actuator force; Vmax the maximal speed of the actuator; $V_{\text{limb}(t)}$ the instantaneous actuator speed; and G the shape factor ¼ 4. The length of the actuator has little influence on force production, and the viscoelastic behavior of attachment structures is not taken into account. Full-scale actuator activation occurs gradually and smoothly (as modeled by a sine-function) and takes 0.02 s. The active state decreases similarly across the time period that corresponds to the final 10% of limb

extension. Numerical forward dynamical modeling of a single kick is performed (Euler integration).The general equation of motion used for both body and feet is discussed by Eq. (2).

$$\text{mass}.a_{(t)} = F_{\text{limb}(t)} + F_{\text{resistive}} \tag{2}$$

'mass' being the representative mass; $a_{(t)}$ the instantaneous acceleration of, respectively, body and feet; $F_{\text{limb}(t)}$ the instantaneous force of the actuator given by (2); and $F_{\text{resistive}}$ the force acting against the movement of body and feet, respectively. Quantifying the locomotor forces that swimming animals experience is a difficult undertaking since it is difficult to directly measure the forces that are delivered to the aquatic medium. Frogs move through the water by using their hindlimbs in unison, which results in high
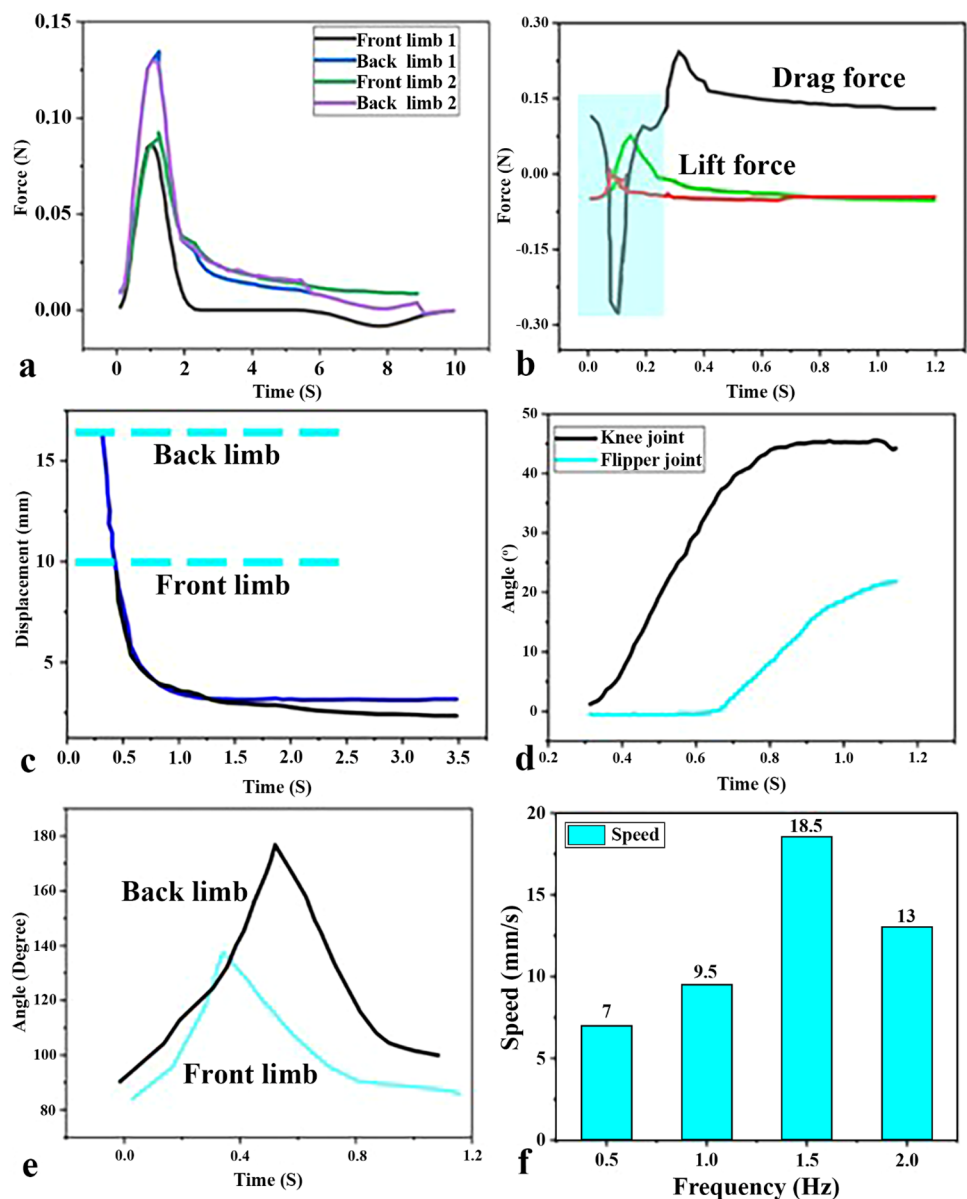
mobility and propulsive efficiency. The following equation is used to determine the drag force acting on the body.

$$F_{DB} = \frac{1}{2} \times \rho \times C_D \times A \times V_B^2 \tag{3}$$

Here, ρ denotes the density of water, C_D: represents the coefficients of drag force, projected area is denoted by A, whereas C_D is the velocity of the body. Moreover, the resultant velocity is given by the following equation.

$$V_{RES} = \sqrt{V_R^2 + V_{NET}^2 + 2 \times V_R \times V_{NET} \times cos\theta} \tag{4}$$

Fig. 4 **a** Force generation of four limbs (front and back) of the proposed FROBOT, **b** drag and lift forces generated by the FROBOT one complete stroke, **c** relaxation capability of back and front limbs, **d** angle actuation against time at two points (knee joint and flipper joint of back limb), **e** angle actuation of front and back limbs in a stroke, **f** speed of the robot at four different frequencies (0.5, 1.0, 1.5, 2.0 Hz)

$$F_{DL} = \frac{1}{2} \times \rho \times C_D \times \sum_{1}^{n} V_{RES}^2 \times \cos(\theta - \beta) \times \left(\frac{(b-a)}{c} \times r_i + a \right) \times \Delta r \qquad (5)$$

$$\beta = Sin^{-1} \left(\frac{V_R}{V_{RES}} \times \sin(\theta) \right) \qquad (6)$$

Drag force acting on leg segments is denoted by F_{DL}.

It is highly pertinent to determine the force each limb generates, which can help to predict the overall swimming performance of robot. For this, a setup was prepared where the each limb was attached to a shaft coupled with load cell. The sensor was interfaced with myRIO, which logged the real-time data after every pre-set sampling time. The process is given in Figure S1. The front limb could create a force of 0.8 N, as illustrated in Fig. 4a, whereas the highest force produced by each back limb was 0.135 N. The robot produced a combined force of 0.4 N. The drag and lift forces produced by the rear limb during a full stroke are seen in Fig. 4b. The robot could only produce a maximum drag force of 0.25 N and a maximum lift force of 0.08 N. Throughout this experiment, a 5 V/1A power source was used. Due to the fact, the muscle wires are actually shape memory alloy. They

retain some energy which resists them to completely return to their initial state. For this Fig. 4c shows the relaxing ability of front and back limb. In the initial few cycles of operation, the limbs return to the ~ 90% of the initial state, however, as the cycles increase the returning ability decreases. Figure 4d shows the angle actuation at two specific points (knee and flipper joints) of back limb. The maximum angle at knee joint reached to 45°, while in case of flipper it was 20°. Moreover, Fig. 4e further analyzes the angle actuated by front and back limbs. The average angles generation by back limb and front limbs were from 80° to 180° and 80° to 145°. The second of the stroke represents the returning of the limbs, which cause the angle to be reduced.

The fabricated robot was then tested in real-time experiments. The nature-inspired setup was prepared with full control using the custom-made software. The swimming experiment was divided into synchronous and asynchronous modes. Further in the later mode, turning right and left was performed. First the FROBOT was tested under different operating frequencies (0.5, 1.0, 1.5 and 2.0 Hz). The
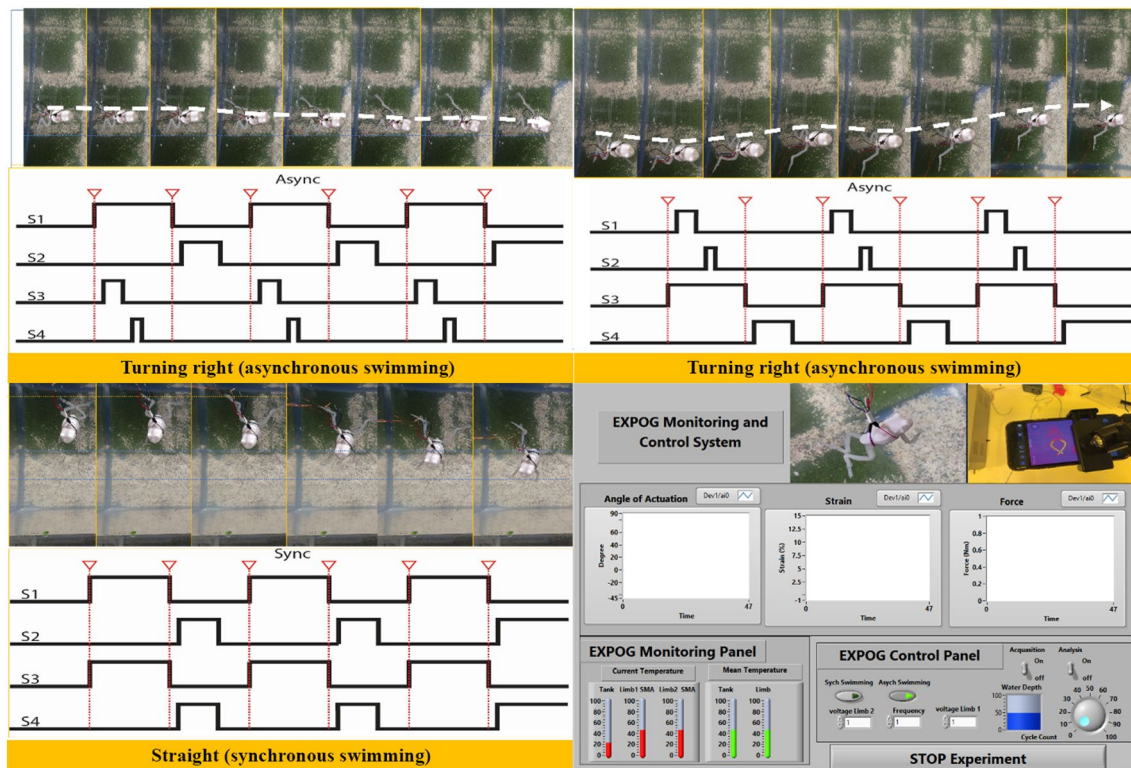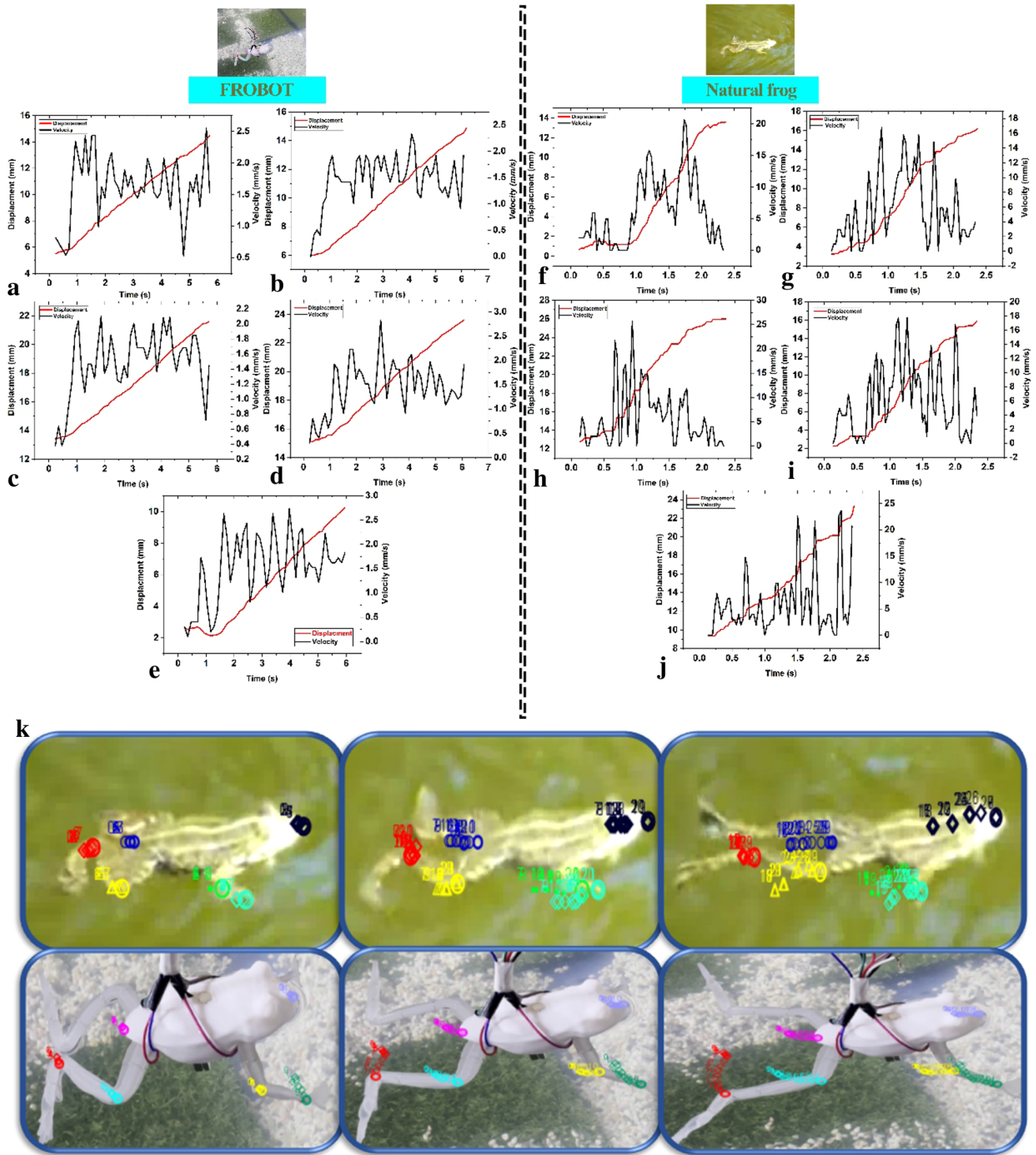

Fig. 5 Continuous frames taken from videos of turning right and its PWM signals for each muscle wire (top left), FROBOT turns left (top right), synchronous swimming (bottom left), custom-made software with monitoring and control features (bottom right)

Fig. 6 Comparison of swimming behavior of proposed FROBOT and real frog; displacement and velocity at five points; ankle joint, flipper end point, front limb joint, frog's head and knee joint of **a–e** FROBOT, **f–j** real frog, **h** the images of FROBOT and real frog with tracked vector points in TRACKER software

application of frequency was pre-calibrated in the software using PWM signals. As the muscle wires are highly dependent on the temperature, which enables the robot to swim at different speeds under different frequencies. Figure 4f

shows the maximum achieved speed of 18 mm/s was at 1.5 Hz. However, increasing the frequency beyond led to only 13 mm/s. As in such case, all the experiments were performed at 1.5 Hz, until mentioned exclusively.

Figure 5 shows the PWM waveforms used for controlling the FROBOT in the respective mode. In the asynchronous mode (turning right), S1 was kept activated while S2 deactivated. However, after the deliberate delay of few milli seconds, the S3 was activated to control the direction. Furthermore, the concept of turning right or left was inspired from the two-wheel line following robots, in which, specific wheel is turned off, in order to move in the direction of blocked wheel. Following the same approach, in the case of turning right, the right limb was deactivated. However, from the practical observation, activating the right limb for the period of 20% duty cycle improved the stability of the robot significantly. Similarly, for turning left, S3 was activated, while S1 activated only for 20% duty cycle. During the whole experiment, the feedback from IR gun for temperature measurement, thermal camera, resistance of the muscle wires and angle of actuation worked as the feedback for the controlled to enable robot swim efficiently. However, for the synchronous swimming, the control was quite simple; S1 and S3 were activated at the same time, while with some delay the antagonistic muscle wires were activated to create the lift force. The bottom right picture in Fig. 5 shows the software that was developed using LabVIEW 2019 and interfaced with myRIO. The user has the liberty to intuitively select the swimming modes, frequency, real-time imaging (thermal and two high-definition cameras) and sensors data. Moreover, all the data were also logged to the computer.

The analysis of swimming locomotion of the proposed FROBOT plays significant role. The swimming pattern must effectively mimic the real frog. For this, the results of the proposed robot were critically compared with that of the real frog. This was made feasible by using a high-definition video of an actual frog for the study. The two-dimensional kinematics were digitally processed to produce video on the large processing device. While the video was framed quickly (at 250 frames per second). The goal was to statistically evaluate both the swimming of a manufactured robot and the position and velocity at a certain spot on the body of a real frog. For this, five points: ankle joint, flipper end point, front limb joint, frog's head and knee joint, were targeted. In the initial stage, vector points were used to automatically trace each frame. Direct linear transformation (DLT) was used in the second step to manually adjust the cleaning of the traced frames, preventing any unintended parallax inaccuracy in the data. After cleaning, the data had a median residual error of 0.35 mm. Due to the enormous amount of frames, only 7 s of the projected FROBOT video and 2.5 s of the actual frog were captured. Figure 6a–e shows the displacement and velocity curves of performed experiment. Whereas Fig. 6f–j shows that of real frog. The position change curves in FROBOT and real frog are increasing with almost linear displacement change. The drag and lift forces that the robot experiences during a power stroke are related to the rise and

fall of this wave's amplitude. It is worth-mentioning that the swimmings gaits are almost similar to that of the real frog. However, the speed is a parameter which is quite slow if compared with the real frog. This is due to the limitation of muscle wires, which take significant time to heat up and then release the time. Due to such case, the operating frequency was limited to 1.5 Hz. The speed was also limited due to opposing forces created by the connecting wires. Even when very tiny wires were employed, their impact was nevertheless felt. Additionally, the suggested robot showed a velocity peak of 2.75 mm/s, when the real frog's velocity peak was far greater at 18 mm/s. Furthermore, the robot moved 9 mm in 7 s, which is far less than the real frog, which moved 16 mm in just 2.5 s. The velocity increased and decreased in step with the magnitude, reaching a maximum peak of 2.75 mm/s at 3 s. This may be the result of the positive force created by the water disturbances caused by the drag and lift forces of the flippers. Figures 6h and S1 show the images of FROBOT and real frog with tracked vector points in TRACKER software. Moreover, swimming comparison of FROBOT and real frog is shown in Figure S2.

4 Conclusion

We propose the design, fabrication and characterization of frog robot (FROBOT) that is capable of swimming underwater in synchronous and asynchronous modes. The robot was designed by printing its muscle wires embedded front and back limbs using PolyJet printing process. Whereas the body of the robot was printed using custom-made multi-header printing system which also placed the muscle wires during the printing phase. Dual thrust approach was implemented which enabled the FROBOT to swimming in both modes with the maximum speed of 18 mm/s at 1.5 Hz. The rigorous analysis of angle of actuation, displacement, velocity curves was performed and compared with that of real frog swimming dynamics. Nature-inspired experimental setup was also designed which was fully controllable using in-house made software. The proposed robot showed remarkable consistency in biomimicking the real frog locomotion with the power supply of 5 V 1A. Moreover, according to the findings, the FROBOT is a promising candidate for bioinspired environmental monitoring.

Declarations

Conflict of interest Authors declare no conflict of interest.

References

1. Soomro, A. M., Khalid, M. A. U., Shah, I., Kim, S. W., Kim, Y. S., & Choi, K. H. (2020). Highly stable soft strain sensor based on Gly-KCl filled sinusoidal fluidic channel for wearable and water-proof robotic applications. *Smart Material and Structures, 29*, 025011. https://doi.org/10.1088/1361-665X/ab540b

2. Pfeil, S., Henke, M., Katzer, K., Zimmermann, M., & Gerlach, G. (2020). A worm-like biomimetic crawling robot based on cylindrical dielectric elastomer actuators. *Frontiers in Robotics AI, 7*, 1–11. https://doi.org/10.3389/frobt.2020.00009

3. Chatterjee, S., Niiyama, R., & Kawahara, Y. (2017). Design and development of a soft robotic earthworm with hydrostatic skeleton. *IEEE International Conference on Robotics and Biomimetics*. https://doi.org/10.1109/ROBIO.2017.8324385. ROBIO 2017. 2018-Janua (2018) 1–6.

4. Jabbar, F., Soomro, A. M., Lee, J., Ali, M., Kim, Y. S., Lee, S., & Choi, K. H. (2020). Robust fluidic biocompatible strain sensor based on pedot : Pss/cnt composite for human-wearable and high-end robotic applications. *Sensors and Materials, 32*, 1–17.

5. Lee, J. W., Soomro, A. M., Waqas, M., Khalid, M. A. U., & Choi, K. H. (2020). A highly efficient surface modified separator fabricated with atmospheric atomic layer deposition for high temperature lithium ion batteries. *International Journal of Energy Research., 44*, 7035–7046. https://doi.org/10.1002/er.5371

6. Ashuri, T., Armani, A., Jalilzadeh Hamidi, R., Reasnor, T., Ahmadi, S., & Iqbal, K. (2020). Biomedical soft robots: current status and perspective. *Biomedical Engineering Letters, 10*, 369–385. https://doi.org/10.1007/s13534-020-00157-6

7. Youn, J. H., Jeong, S. M., Hwang, G., Kim, H., Hyeon, K., Park, J., & Kyung, K. U. (2020). Dielectric elastomer actuator for soft robotics applications and challenges. *Applied Sciences, 10*, 1–31. https://doi.org/10.3390/app10020640

8. Marchese, A. D., Onal, C. D., & Rus, D. (2014). Autonomous soft robotic fish capable of escape maneuvers using fluidic elastomer actuators. *Soft Robotics, 1*, 75–87. https://doi.org/10.1089/soro.2013.0009

9. Liu, Y., Qiao, Y., Zhang, Y., Yang, Z., Gao, T., Kirsch, D., Liu, B., Song, J., Yang, B., & Hu, L. (2018). 3D printed separator for the thermal management of high-performance Li metal anodes. *Energy Storage Materials, 12*, 197–203. https://doi.org/10.1016/j.ensm.2017.12.019

10. Agaoglu, S., Diep, P., Martini, M., Samudhyatha, K. T., Baday, M., & Araci, I. E. (2018). Ultra-sensitive microfluidic wearable strain sensor for intraocular pressure monitoring. *Lab on a Chip, 18*, 3471–3483. https://doi.org/10.1039/c8lc00758f

11. Boateng, B., Zhu, G., Lv, W., Chen, D., Feng, C., Waqas, M., Ali, S., Wen, K., & He, W. (2018). An Efficient, Scalable Route to Robust PVDF-co-HFP/SiO 2 Separator for Long-Cycle Lithium Ion Batteries, *Physica Status Solidi. Lett., 12*, 2–7. https://doi.org/10.1002/pssr.201800319

12. Katzschmann, R. K., DelPreto, J., MacCurdy, R., & Rus, D. (2018). Exploration of underwater life with an acoustically controlled soft robotic fish. *Science Robotics, 3*, 1–13. https://doi.org/10.1126/SCIROBOTICS.AAR3449

13. Du, T., Hughes, J., Wah, S., Matusik, W., & Rus, D. (2021). Underwater soft robot modeling and control with differentiable simulation. *IEEE Robotics and Automation Letters, 6*, 4994–5001. https://doi.org/10.1109/LRA.2021.3070305

14. Ulloa, C. C., Terrile, S., & Barrientos, A. (2020). Soft underwater robot actuated by shape-memory alloys "jellyrobcib" for path tracking through fuzzy visual control. *Applied Sciences, 10*, 1–22. https://doi.org/10.3390/app10207160

15. Joshi, A., Kulkarni, A., & Tadesse, Y. (2019). FludoJelly: Experimental study on jellyfish-like soft robot enabled by soft pneumatic composite (SPC). *Robotics*. https://doi.org/10.3390/robotics8030056

16. Choi, J., Ahn, S. H., & Cho, K. J. (2020). Design of fully soft actuator with double-helix tendon routing path for twisting motion. *IEEE International Conference of Intelligent Robotics Systems*. https://doi.org/10.1109/IROS45743.2020.9341363

17. Rodrigue, H., Wang, W., Han, M. W., Kim, T. J. Y., & Ahn, S. H. (2017). An overview of shape memory alloy-coupled actuators and robots. *Soft Robotics, 4*, 3–15. https://doi.org/10.1089/soro.2016.0008

18. Zhang, R. Z., Shen, Z., & Wang, Z. (2018). Ostraciiform underwater robot with segmented caudal fin. *IEEE International Conference on Robotics Systems, 3*, 2902–2909. https://doi.org/10.1109/LRA.2018.2847198

19. Copaci, D., Martin, F., Moreno, L., & Blanco, D. (2019). SMA based elbow exoskeleton for rehabilitation therapy and patient evaluation. *IEEE Access, 7*, 31473–31484. https://doi.org/10.1109/ACCESS.2019.2902939

20. Copaci, D., Cano, E., Moreno, L., & Blanco, D. (2017). New design of a soft robotics wearable elbow exoskeleton based on shape memory alloy wire actuators. *Applied Bionics and Biomechanics, 2017*, 1605101. https://doi.org/10.1155/2017/1605101

21. Cianchetti, M., Laschi, C., Menciassi, A., & Dario, P. (2018). Biomedical applications of soft robotics. *Nature Reviews Materials, 3*, 143–153. https://doi.org/10.1038/s41578-018-0022-y

22. Zhakypov, Z., Huang, J. L., & Paik, J. (2016). A novel torsional shape memory alloy actuator: Modeling, characterization, and control. *IEEE Robotics and Automation Megazine, 23*, 65–74. https://doi.org/10.1109/MRA.2016.2582868

23. Zhao, W. C., Zhang, Y., & Wang, N. (2021). Soft robotics: research, challenges, and prospects. *Journal of Robotics and Mechatronics, 33*, 45–68. https://doi.org/10.20965/jrm.2021.p0045

24. Simone, F., Rizzello, G., Seelecke, S., & Motzki, P. (2020). A soft five-fingered hand actuated by shape memory alloy wires: Design, manufacturing, and evaluation. *Frontiers in Robotics and AI*. https://doi.org/10.3389/frobt.2020.608841

25. Copaci, D., Munõz, J., González, I., Monje, C. A., & Moreno, L. (2020). SMA-driven soft robotic neck: Design, control and validation. *IEEE Access., 8*, 199492–199502. https://doi.org/10.1109/ACCESS.2020.3035510

26. Wang, W., Yu, C. Y., Abrego Serrano, P. A., & Ahn, S. H. (2020). Shape memory alloy-based soft finger with changeable bending length using targeted variable stiffness. *Soft Robotics., 7*, 283–291. https://doi.org/10.1089/soro.2018.0166

27. Shintake, J., Schubert, B., Rosset, S., Shea, H., & Floreano, D. (2015). Variable stiffness actuator for soft robotics using dielectric elastomer and low-melting-point alloy. In *IEEE International conference on robotics systems*, Hamburg, Germany (pp. 1097–1102). https://doi.org/10.1109/IROS.2015.7353507.

28. Copaci, D. S., Blanco, D., Martin-Clemente, A., & Moreno, L. (2020). Flexible shape memory alloy actuators for soft robotics: Modelling and control. *International Journal of Advanced Robotics Systems, 17*, 1–15. https://doi.org/10.1177/1729881419886747

29. Liu, M. F., Hao, L. N., Zhang, W., & Zhao, Z. R. (2020). A novel design of shape-memory alloy-based soft robotic gripper with

variable stiffness. *International Journal of Advanced Robotics Systems*, *17*, 1–12. https://doi.org/10.1177/1729881420907813

30. Soomro, A. M., Shah, M. A., Memon, A. P., Abro, S., & Soomro, S. A. (2016). Performance assessment of thyristor controlled series compensator considering various circuit parameters using voltage and current steady-state equations on simulink. *Sindh University Research Journal (Science Ser)*, *48*(4), 787–792.

31. Waqas, M., Soomro, A. M., Ali, S., Ashraf, H., Chan, A. S., Kumar, S., & Choi, K. H. (2021). A highly efficient composite separator embedded with colloidal lanthanum oxide nanocrystals for high-temperature lithium-ion batteries. *International Journal of Energy Research, 45*, 11179–11192. https://doi.org/10.1002/er.6599

32. Soomro, A. M., Jabbar, F., Ali, M., Lee, J. W., Mun, S. W., & Choi, K. H. (2019). All-range flexible and biocompatible humidity sensor based on poly lactic glycolic acid (PLGA) and its application in human breathing for wearable health monitoring. *Journal of Materials: Materials in Electronics, 30*, 9455–9465. https://doi.org/10.1007/s10854-019-01277-1

33. Khalid, M. A. U., Kim, S. W., Lee, J., Soomro, A. M., Rehman, M. M., Lee, B. G., & Choi, K. H. (2020). Resistive switching device based on SrTiO3/PVA hybrid composite thin film as active layer. *Polymer, 189*, 122183. https://doi.org/10.1016/j.polymer.2020.122183

34. Soomro, A. M., Lee, J. W., Waqas, M., Kim, Y. S., Ali, M., Khalid, M. A. U., & Choi, K. H. (2020). A robust surface-modified separator fabricated with roll-to-roll atomic layer deposition and electrohydrodynamic deposition techniques for high temperature lithium ion batteries. *Journal of Electrochemical Society, 167*, 160507. https://doi.org/10.1149/1945-7111/abca71

35. Schmitt, F., Piccin, O., Barbé, L., & Bayle, B. (2018). Soft robots manufacturing: A review. *Frontiers in Robotics and AI*. https://doi.org/10.3389/frobt.2018.00084

36. Shen, Z., Na, J., & Wang, Z. (2017). A biomimetic underwater soft robot inspired by cephalopod mollusc. *IEEE Automation and Robotics Letter, 2*, 2217–2223. https://doi.org/10.1109/LRA.2017.2724760

37. Lee, J. H., Chung, Y. S., & Rodrigue, H. (2019). Long shape memory alloy tendon-based soft robotic actuators and implementation as a soft gripper. *Scientific Reports, 9*, 11251. https://doi.org/10.1038/s41598-019-47794-1

38. Shintake, J., Rosset, S., Schubert, B., Mintchev, S., Floreano, D., & Shea, H. R. (2015). DEA for soft robotics: 1-gram actuator picks up a 60-gram egg. *Electroactive Polymer and Actuators Devices, 2015*(9430), 94301S. https://doi.org/10.1117/12.2084043

39. Boyraz, P., Runge, G., & Raatz, A. (2018). An overview of novel actuators for soft robotics. *Actuators, 7*, 1–21. https://doi.org/10.3390/act7030048

40. Duduta, M., Berlinger, F., Nagpal, R., Clarke, D. R., Wood, R. J., & Temel, F. Z. (2020). Tunable multi-modal locomotion in soft dielectric elastomer robots. *IEEE Automation and Robotics Letter, 5*, 3868–3875. https://doi.org/10.1109/LRA.2020.2983705

41. Shintake, J., Shea, H., & Floreano, D. (2016). Biomimetic underwater robots based on dielectric elastomer actuators. *IEEE International Conference on Robotics Systems*. https://doi.org/10.1109/IROS.2016.7759728. 2016-Novem 4957–4962.

42. Christianson, C., Goldberg, N. N., Deheyn, D. D., Cai, S., & Tolley, M. T. (2018). Translucent soft robots driven by frameless fluid electrode dielectric elastomer actuators. *Science Robotics, 3*, 1–9. https://doi.org/10.1126/SCIROBOTICS.AAT1893